Electron-momentum distributions and photoelectron spectra of atoms driven by an intense spatially inhomogeneous field

M. F. Ciappina,[1,2] J. A. Pérez-Hernández,[3] T. Shaaran,[1] L. Roso,[3] and M. Lewenstein[1,4]

[1]*ICFO-Institut de Ciències Fotòniques, Mediterranean Technology Park, 08860 Castelldefels (Barcelona), Spain*
[2]*Department of Physics, Auburn University, Auburn, Alabama 36849, USA*
[3]*Centro de Láseres Pulsados (CLPU), Parque Científico, 37185 Villamayor, Salamanca, Spain*
[4]*ICREA-Institució Catalana de Recerca i Estudis Avançats, Lluis Companys 23, 08010 Barcelona, Spain*

We use the three-dimensional time-dependent Schrödinger equation (3 D-TDSE) to calculate angular electron momentum distributions and photoelectron spectra of atoms driven by spatially inhomogeneous fields. An example for such inhomogeneous fields is the locally enhanced field induced by resonant plasmons, appearing at surfaces of metallic nanoparticles, nanotips, and gold bow-tie shaped nanostructures. Our studies show that the inhomogeneity of the laser electric field plays an important role on the above-threshold ionization process in the tunneling regime, causing significant modifications on the electron momentum distributions and photoelectron spectra, while its effects in the multiphoton regime appear to be negligible. Indeed, through the tunneling above-threshold ionization (ATI) process, one can obtain higher energy electrons as well as a high degree of asymmetry in the momentum space map. In this study we consider near infrared laser fields with intensities in the mid- 10^{14} W/cm^2 range and we use a linear approximation to describe their spatial dependence. We show that in this case it is possible to drive electrons with energies in the near-keV regime. Furthermore, we study how the carrier envelope phase influences the emission of ATI photoelectrons for few-cycle pulses. Our quantum mechanical calculations are fully supported by their classical counterparts.

I. INTRODUCTION

The process known as above-threshold ionization (ATI), in which an atom or molecule absorbs more photons than the minimum number required to single ionize it, has been a subject of intensive studies during the last decades (see, e.g., [1] and references therein). The first experimental realization was made at the end of the 1970s [2] and since then there has been truly amazing progress in the understanding of the nonperturbative nature of ATI. The recent advances in laser technology make it possible to routinely generate laser pulses with a few cycles of duration, which allows control of the atomic and molecular processes in their natural time scales, i.e., in the range of (sub)-femto to attoseconds. In addition, these short laser sources find an extensive range of applications in basic science, such as controlling molecular motions and chemical reactions [3,4]. Furthermore, the few-cycles pulses provide the fundamental pillar in the generation of high-order harmonics and the creation of isolated extreme ultraviolet (XUV) pulses [5,6].

The appearance of COLTRIMS experiments (see, e.g., [7] and references therein) offered an unprecedented possibility of performing stringent tests on the different theoretical approaches. On one side, this is because the imaging of the vectorial momentum distributions of the reaction fragments are easily accessible, while on the other they are particularly sensitive to various details of the theory. COLTRIMS were primarily developed for the study of few-body dynamics induced by particle impact, i.e., electrons and ions, but the extension to scrutinize and tackle laser-induced processes was natural (see, e.g., [8–10]). Among the features which were theoretically analyzed was the complex emission pattern present in the two-dimensional momentum plane, parallel and perpendicular to the laser polarization axis, of the laser-ionized electron

distributions near threshold [11]. It was also investigated how these patterns evolve as the laser-matter processes change from the multiphoton to the tunneling regimes [10].

The main difference between a few-cycle pulse and a multicycle one is the strong dependence of the laser electric field on the so-called carrier envelope phase (CEP) [12,13]. The electric field in a few-cycle pulse can be characterized by its duration and by the CEP. The influence of CEP has been experimentally observed in high-harmonic generation (HHG) [14], the emission direction of electrons from atoms [15], and in the yield of nonsequential double ionization [16]. In order to have a better control of the system on an attosecond temporal scale it is, therefore, important to find reliable and direct schemes to measure the absolute phase of few-cycle pulses.

The investigation of ATI generated by few-cycle driving laser pulses plays a key role in the CEP characterization due to the sensitivity of the energy and angle-resolved photoelectron spectra to the value of the laser electric field absolute phase [17,18]. Consequently, the behavior of the laser-ionized electrons renders the ATI phenomenon a very valuable tool for laser pulse characterization. To determine the CEP of a few-cycle laser pulse, it is essential to record the difference between the yield of electrons ionized for different emission angles. Through this technique one can analyze the so-called backward-forward asymmetry in order to characterize the absolute CEP of a few-cycle laser pulse [19]. Furthermore, it appears that the high-energy region of the photoelectron spectra is most sensitive to the absolute CEP and consequently electrons with large kinetic energy are needed in order to correctly describe it [1,20].

Recent experiments using a combination of plasmonic nanostructures and rare gases have demonstrated that the

harmonic cutoff of the gases could be extended further than in conventional situations by using the field locally enhanced due to the coupling of a laser pulse with the metal nanostructure [21,22]. In such nanosystems, due to the strong confinement of the plasmonics spots and the distortion of the electric field by the surface plasmons, the locally enhanced field is not spatially homogeneous in the region where the electron dynamics takes place. One should note, however, that the outcome of the experiments of Ref. [21], in which a combination of gold bow-tie nanostructure and argon gas for generation HHG was used, has been recently under intense scrutiny [23,24]. In addition, recently, instead of atoms or molecules in gas phase, solid state nanostructures have been employed as a target to study the photoelectron emission by intense few-cycle laser pulses [25,26]. This laser driven phenomenon, called above-threshold photoemission (ATP), has received special attention due to the novelty of the involved physics and potential applications. In the ATP process, the emitted electrons have energy far beyond the usual cutoff for noble gases (see, e.g., [26–31]). Furthermore, the photoelectrons emitted from these nanosources are sensitive to the CEP, and consequently this fact plays an important role in the angle and energy-resolved photoelectron spectra [25,26,32,33].

From a theoretical point of view, the fundamental assumption behind all the strong field phenomena, namely that the laser field is spatially homogeneous in the region where the electron dynamics takes place [34,35], is not any more valid for the locally enhanced plasmonic field. Indeed, in such system the driven electric field, and consequently the Lorentz force the laser-ionized electron feels, will also depend on position. Up to now there have been very few studies investigating the strong field phenomena in such spatially inhomogeneous fields [36–42]. All of these studies have demonstrated that the spatial dependency of the field strongly modifies the laser-driven phenomena that appear in such circumstances.

For a homogeneous driving field, up to know, different numerical and analytical approaches have been employed to calculate the ATI (see, e.g., [1,43–47] and references therein). In this article we extend the studies of our previous paper [40] by applying the numerical solution of the time-dependent Schrödinger equation (TDSE) in three dimensions to calculate the angular electron momentum distributions and photoelectron spectra of ATI driven by spatially inhomogeneous fields, covering both the tunneling and multiphoton regimes. The spatial dependence of the field is considered to be linear and this can be considered a reliable approximation in the parameters range we use in the present article [36–42]. We mainly focus on studying ATI of hydrogen atoms, but our scheme, within the single active electron approximation, can be directly applied to any complex atom. We demonstrate how the spatial inhomogeneity of the laser electric field modifies both the two-dimensional electron momentum distributions and the photoelectron spectra. In addition, we examine also the influence of the CEP parameter in the measurable quantities. Finally, our quantum mechanical results are compared with classical calculations based on Newton equations.

This article is organized as follows. In the next section we present our theoretical approach to model ATI driven by spatially nonhomogeneous fields, with main emphasis on the extraction of the electron angular momentum distributions

starting from the TDSE outcomes. Subsequently, in Sec. III we apply our method to compute the electron momentum distributions and energy-resolved photoelectron spectra of hydrogen atoms using few-cycle laser pulses for both homogeneous and inhomogeneous fields, considering the tunneling and multiphoton regimes. Furthermore, we solve the classical equations of motion of an electron in an oscillating inhomogeneous electric field to support our quantum mechanical method. Finally, in Sec. IV we conclude our contributions with a short summary and outlook.

II. THEORETICAL APPROACH

In order to obtain the characteristics of the above-threshold ionization (ATI) phenomenon driven by spatial nonhomogeneous fields, such as the electron momentum distribution and the energy-resolved photoelectron spectra $P(E)$ (including the dynamics of both direct and rescattered electrons), we solve the three-dimensional time-dependent Schrödinger equation (3D-TDSE) in the length gauge:

$$i\frac{\partial \Psi(\mathbf{r},t)}{\partial t} = H\Psi(\mathbf{r},t) = \left[-\frac{\nabla^2}{2} - \frac{1}{r} + V_l(\mathbf{r},t) \right]\Psi(\mathbf{r},t). \quad (1)$$

The time-dependent electronic wave function $\Psi(\mathbf{r},t)$ can be expanded in terms of spherical harmonics:

$$\Psi(\mathbf{r},t) = \Psi(r,\theta,\phi,t) \approx \sum_{l=0}^{L-1}\sum_{m=-l}^{l}\frac{\Phi_{lm}(r,t)}{r}Y_l^m(\theta,\phi), \quad (2)$$

where the number of partial waves depends on each specific case. Here, in order to assure the numerical convergence, we have used up to $L \approx 250$ in the most extreme case ($I = 5.0544 \times 10^{14}$ W/cm^2). In addition, due to the fact that the plasmonic field is linearly polarized, the magnetic quantum number is conserved and consequently in the following we can consider only $m = 0$ in Eq. (2). This property considerably reduces the complexity of the problem. In here we consider z as a polarization axis and we take into account that the
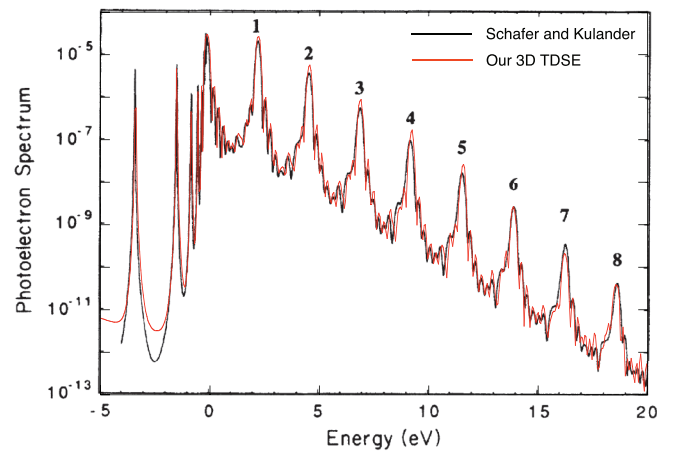

FIG. 1. (Color online) Photoelectron spectrum resulting from our 3D-TDSE simulations (in red) and superimposed (in black) with the ATI results calculated by Schafer and Kulander in Ref. [48]. The laser wavelength is $\lambda = 532$ nm and the intensity is $I = 2 \times 10^{13}$ W/cm^2 (see Fig. 1 in [48] for more details). The superimposed plot has been extracted from Fig. 1 of this cited reference.
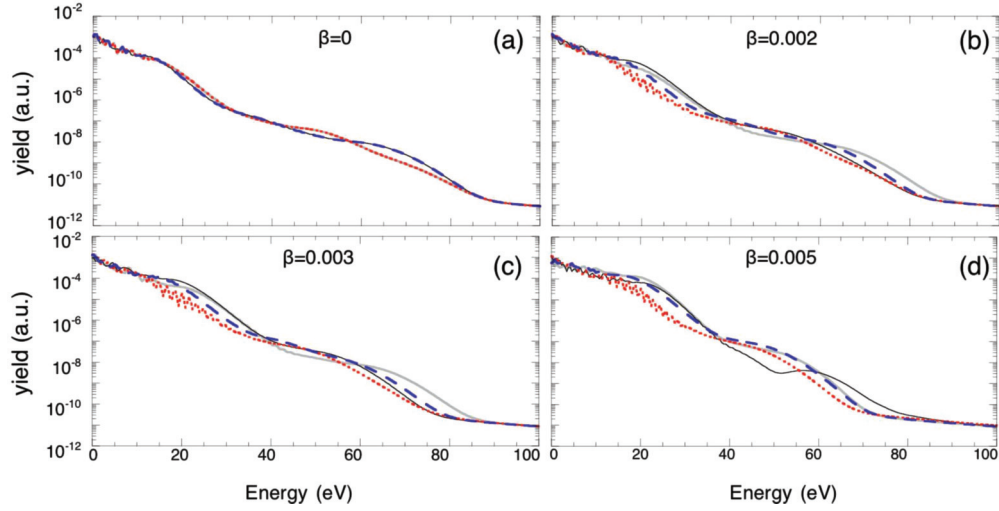
FIG. 2. (Color online) Energy-resolved photoelectron spectra $P(E)$ calculated using the 3D-TDSE for an hydrogen atom ($I_p = -0.5$ a.u.). The laser parameters are $I = 1.140 \times 10^{14}$ W/cm^2 ($E_0 = 0.057$ a.u.) and $\lambda = 800$ nm. We have used a sin-squared shaped pulse with a total duration of four optical cycles (10 fs). (a) $\beta = 0$ (homogeneous case), (b) $\beta = 0.002$, (c) $\beta = 0.003$, and (d) $\beta = 0.005$. In all panels, solid gray line: $\phi = 0$; solid black line $\phi = \pi/2$; dotted red line: $\phi = \pi$; and dashed blue line: $\phi = 3\pi/2$.

spatial variation of the electric field is linear with respect to the position. As a result, the coupling $V_l(\mathbf{r},t)$ between the atomic electron and the electromagnetic radiation reads

$$V_l(\mathbf{r},t) = \int^{\mathbf{r}} d\mathbf{r}' \cdot \mathbf{E}(\mathbf{r}',t) = E_0 z(1 + \beta z) f(t) \sin(\omega t + \phi),$$
(3)

where E_0, ω, and ϕ are the laser electric field amplitude, the central frequency, and the carrier envelope phase (CEP), respectively. The parameter β defines the "strength" of the inhomogeneity and has units of inverse length (see also [36–38]). For modeling short laser pulses in Eq. (3), we use a sin-squared envelope $f(t)$ of the form

$$f(t) = \sin^2\left(\frac{\omega t}{2n_p}\right),$$
(4)

where n_p is the total number of optical cycles. As a result, the total duration of the laser pulse will be $T_p = n_p \tau$, where $\tau = 2\pi/\omega$ is the laser period. We also assume that before switch on of the laser ($t = -\infty$) the target atom (hydrogen) is in its ground state ($1s$), whose analytic form can be found in standard textbooks. Within the single active electron approximation, however, our numerical scheme is tunable to treat any complex atom by choosing the adequate effective (Hartree-Fock) potential, and finding the ground state by numerical diagonalization.

Next, we will show how the inhomogeneity modifies the equations which model the laser-electron coupling. Inserting Eq. (2) into Eq. (1) and considering that

$$\cos\theta Y_l^0 = c_{l-1} Y_{l-1}^0 + c_l Y_{l+1}^0,$$
(5)

$$\cos^2\theta Y_l^0 = c_{l-2} c_{l-1} Y_{l-1}^0 + \left(c_{l-1}^2 + c_l^2\right) Y_l^0 + c_l c_{l+1} Y_{l+2}^0,$$
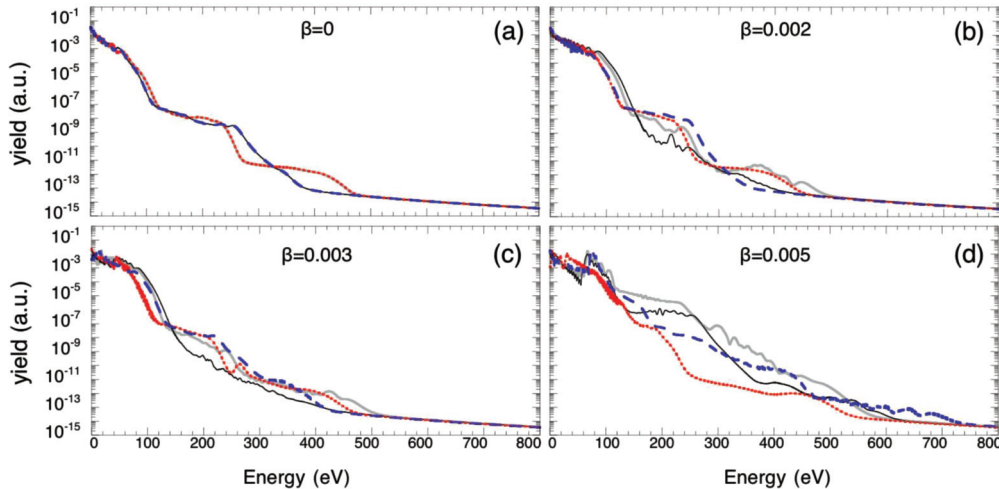(6)

FIG. 3. (Color online) Idem Fig. 2 but for a laser intensity $I = 5.404 \times 10^{14}$ W/cm^2 ($E_0 = 0.12$ a.u.).
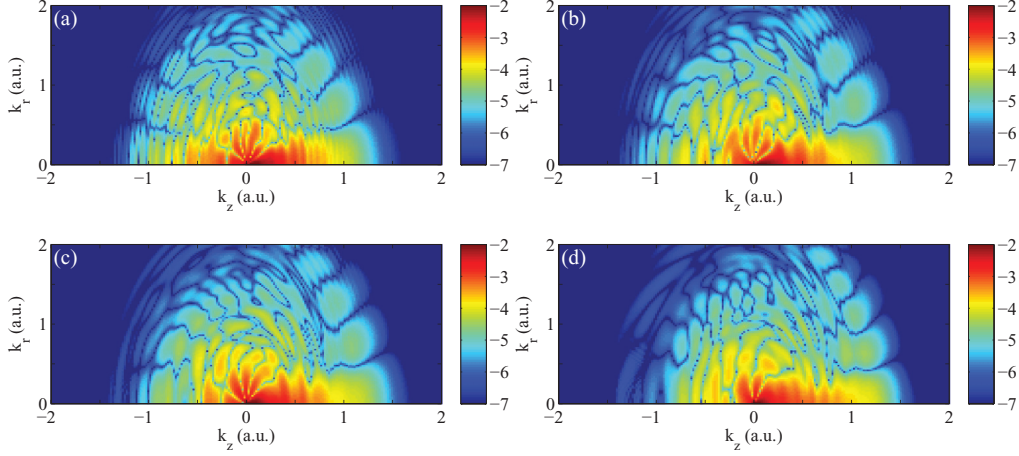
FIG. 4. (Color online) Two-dimensional electron momentum distributions (logarithmic scale) in cylindrical coordinates (k_z, k_r) using the exact 3D-TDSE calculation for an hydrogen atom. The laser parameters are $I = 1.140 \times 10^{14}$ W/cm^2 ($E_0 = 0.057$ a.u.) and $\lambda = 800$ nm. We have used a sin-squared shaped pulse with a total duration of four optical cycles (10 fs) with $\phi = 0$. (a) $\beta = 0$ (homogeneous case), (b) $\beta = 0.002$, (c) $\beta = 0.003$, and (d) $\beta = 0.005$.

where

$$c_l = \sqrt{\frac{(l+1)^2}{(2l+1)(2l+3)}}, \tag{7}$$

we obtain a set of coupled differential equations for each of the radial functions $\Phi_l(r,t)$:

$$
\begin{aligned}
i\frac{\partial \Phi_l}{\partial t} = &\left[-\frac{1}{2}\frac{\partial^2}{\partial r^2} + \frac{l(l+1)}{2r^2} - \frac{1}{2} \right]\Phi_l \\
&+ \beta r^2 E(t)\big(c_l^2 + c_{l-1}^2\big)\Phi_l \\
&+ r E(t)(c_{l-1}\Phi_{l-1} + c_l\Phi_{l+1}) \\
&+ \beta r^2 E(t)(c_{l-2}c_{l-1}\Phi_{l-2} + c_l c_{l+1}\Phi_{l+2}). \tag{8}
\end{aligned}
$$

Equation (8) is solved using the Crank-Nicolson algorithm considering the additional term, i.e., Eq. (6) due to the spatial inhomogeneity.

The ATI spectrum is calculated using the time-dependent wave function method developed by Schafer and Kulander (see [48] for more details). As a preliminary test and in order to assure the consistence of our numerical simulations, we have checked out our calculations with the results previously obtained in Ref. [48]. The comparison confirms the high degree of accuracy of our calculations as shown in Fig. 1.

For calculating the energy-resolved photoelectron spectra $P(E)$ and two-dimensional electron distributions $\mathcal{H}(p,\theta)$ we use the window function approach developed by Schafer [48,49]. This tool has been widely used, both to calculate angle-resolved and energy-resolved photoelectron spectra [50], and it represents a step forward with respect to the usual projection methods.

III. RESULTS

In this section we calculate both energy-resolved photoelectron spectra $P(E)$ and two-dimensional electron momentum distributions in order to investigate the influence of the spatial inhomogeneities of the field and the sensitivity of these two measurable quantities to the different laser parameters, especially to the carrier envelope phase (CEP). The investigations
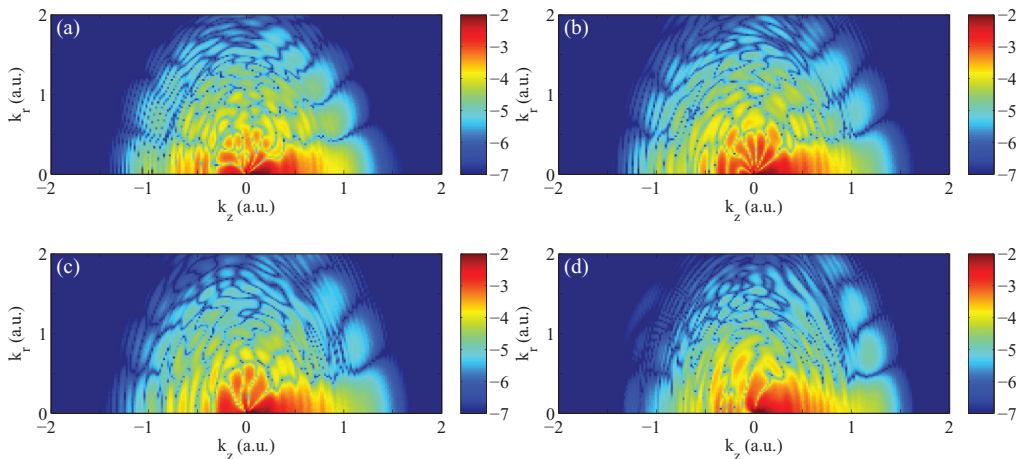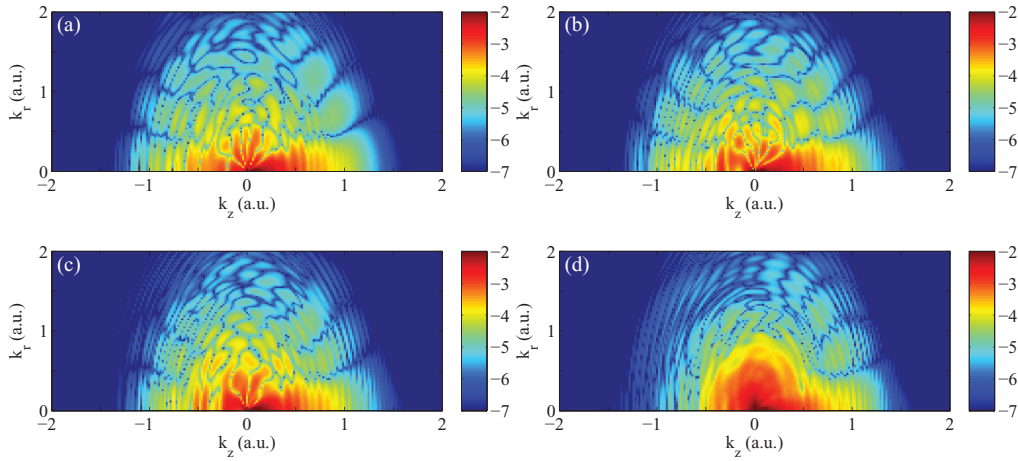

FIG. 5. (Color online) Idem Fig. 4 but for $\phi = \pi/2$.
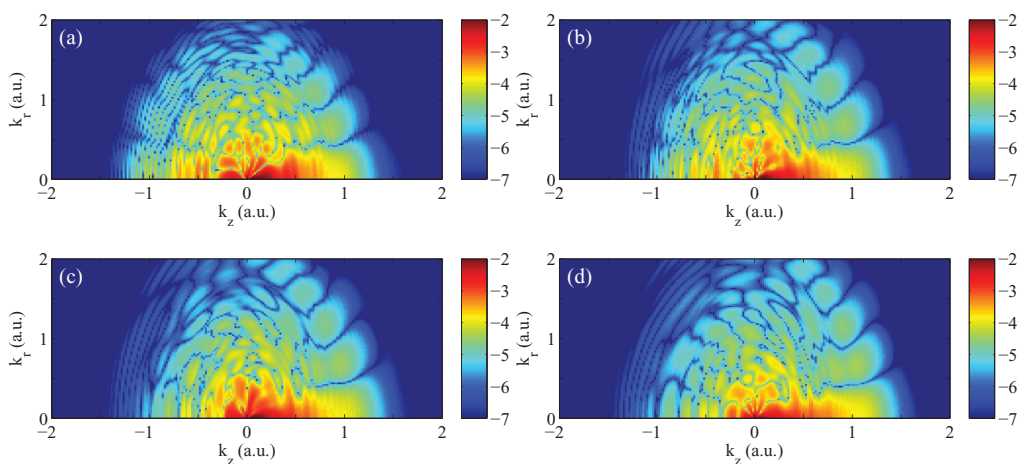
FIG. 6. (Color online) Idem Fig. 4 but for $\phi = \pi$.

are carried out for both the tunneling, for which the Keldysh parameter is $\gamma \lesssim 1$ ($\gamma = \sqrt{I_p/2U_p}$, where $U_p = I/4\omega^2$ is the ponderomotive energy and I_p is the ionization potential), and multiphoton regimes, for which the Keldysh parameter is $\gamma \gg 1$. Furthermore, we confirm how in the tunneling regime the CEP, joint with the spatial nonhomogeneities, modify in a particular way both the energy-resolved photoelectron spectra and the two-dimensional electron momentum distributions as we have shown in our previous contribution [40]. On the other hand, we show that in the multiphoton regime ($\gamma \gg 1$) the spatial nonhomogeneous character of the laser electric field hardly affects the analyzed quantities. We also want to point out, however, that the frontier between the tunnel and multiphoton regimes appears to be a controversial and diffuse issue [51,52].

A. Tunneling regime

We commence by investigating the tunneling regime. For this case we employ a four-cycle (total duration 10 fs) sin-squared laser pulse with wavelength $\lambda = 800$ nm and two different intensities, namely $I = 1.140 \times 10^{14}$ W/cm^2 and $I = 5.0544 \times 10^{14}$ W/cm^2. These two intensities give

values for the laser electric field of $E_0 = 0.057$ a.u. and $E_0 = 0.12$ a.u., respectively. For all the cases we chose four different values for the parameter that characterizes the inhomogeneity strength, namely, $\beta = 0$ (homogeneous case), $\beta = 0.002$, $\beta = 0.003$, and $\beta = 0.005$. In addition we also vary the carrier envelope phase ϕ in Eq. (3), taking $\phi = 0$, $\phi = \pi/2$, $\phi = \pi$, and $\phi = 3\pi/2$. For all the above mentioned cases we calculate the so-called energy-resolved photoelectron spectra $P(E)$ [1]. The results are shown in Figs. 2 and 3 for $I = 1.140 \times 10^{14}$ W/cm^2 ($\gamma = 1$) and $I = 5.0544 \times 10^{14}$ W/cm^2 ($\gamma = 0.475$), respectively.

For the homogeneous case, the spectra exhibits the usual distinct behavior, namely, the $2U_p$ cutoff [≈ 13.6 eV in Fig. 2(a) and ≈ 57.4 eV in Fig. 3(a)] and the $10U_p$ cutoff [≈ 68 eV in Fig. 2(a) and ≈ 300 eV in Fig. 3(a)]. The former cutoff corresponds to those electrons that, once ionized, never return to the atomic core (the so-called *direct* electrons), while the latter one corresponds to the electrons that, once ionized, return to the parent ion and elastically rescatter (the so-called *rescattered* electrons). Classically, it is a well established fact that the maximum kinetic energies E_k of the direct and the rescattered electrons are $E_{\max}^d = 2U_p$ and $E_{\max}^r = 10U_p$, respectively (see below for more details). In a quantum

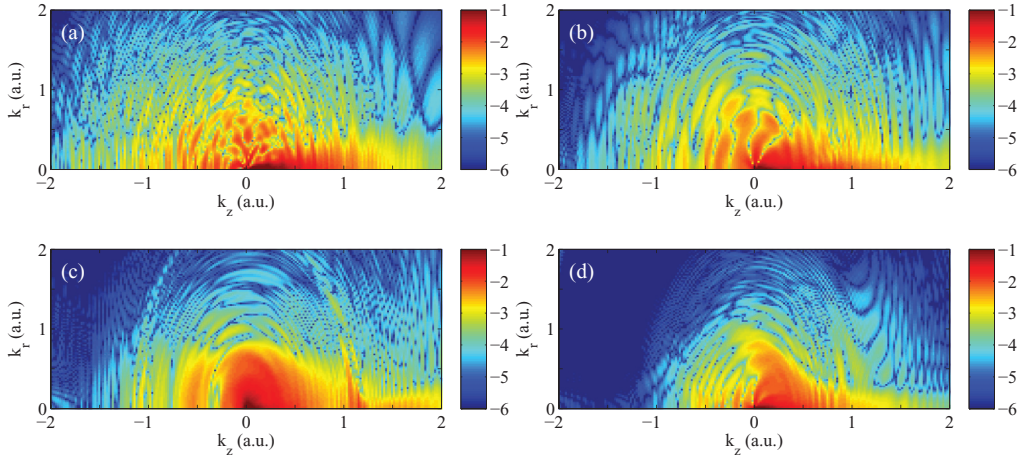FIG. 7. (Color online) Idem Fig. 4 but for $\phi = 3\pi/2$.

FIG. 8. (Color online) Two-dimensional electron momentum distributions (logarithmic scale) in cylindrical coordinates (k_z, k_r) using the exact 3D-TDSE calculation for an hydrogen atom. The laser parameters are $I = 5.0544 \times 10^{14}$ W/cm^2 ($E_0 = 0.12$ a.u.) and $\lambda = 800$ nm. We have used a sin-squared shaped pulse with a total duration of four optical cycles (10 fs) with $\phi = 0$. (a) $\beta = 0$ (homogeneous case), (b) $\beta = 0.002$, (c) $\beta = 0.003$, and (d) $\beta = 0.005$.

mechanical approach, however, it is possible to find electrons with energies beyond the $10U_p$ cutoff, although their yield drops several orders of magnitude depending strongly on the atomic species studied [1].

Experimentally speaking, both the direct and rescattered electrons contribute to the energy-resolved photoelectron spectra. It means for tackling this problem both physical mechanisms should be included in any theoretical model. In that sense, the 3D-TDSE, which can be considered as an exact approach to the ATI problem for atoms and molecules in the single active electron approximation, appears to be the adequate tool to predict the $P(E)$ in the whole range of electron energies. On the other hand, the most energetic electrons, i.e., those with kinetic energies $E_k \gg 2U_p$, are commonly used to characterize the CEP of few-cycle pulses. Consequently, if one will use the high energy region of the $P(E)$ to compute the absolute CEP, a correct description of the electron rescattering mechanism is necessary.

For the spatially nonhomogeneous cases, the positions of the direct and the rescattered electron cutoffs are extended

towards larger energies. For the rescattered electrons, this extension is very noticeable. In fact for $\beta = 0.005$ with $E_0 = 0.12$ a.u., it reaches values close to ≈ 700 eV [Fig. 3(d)] against the ≈ 300 eV shown by the homogeneous case [Fig. 3(a)]. Another new feature present for all the nonhomogeneous cases is the strong sensitivity of the $P(E)$ to the carrier envelope phase (CEP). This behavior can be clearly noticed by comparing Figs. 2(a) and 3(a) (i.e., the homogeneous case) with the rest of the panels of Figs. 2 and 3. It is evident that for the homogeneous case only two curves are present, due to the fact that the $P(E)$ for $\phi = 0$ ($\phi = \pi/2$) is identical to $\phi = \pi$ ($\phi = 3\pi/2$), respectively. On the other hand, for all the nonhomogeneous cases it is possible to clearly distinguish the four cases, i.e., $\phi = 0$ (solid gray lines), $\phi = \pi/2$ (solid black lines), $\phi = \pi$ (dotted red lines), and $\phi = 3\pi/2$ (dashed blue lines). Indeed, this particular characteristic of the $P(E)$ for nonhomogeneous fields could make them a new and better CEP characterization tool.

It should be noted, however, that other well-known and established CEP characterization tools, such as, for instance,
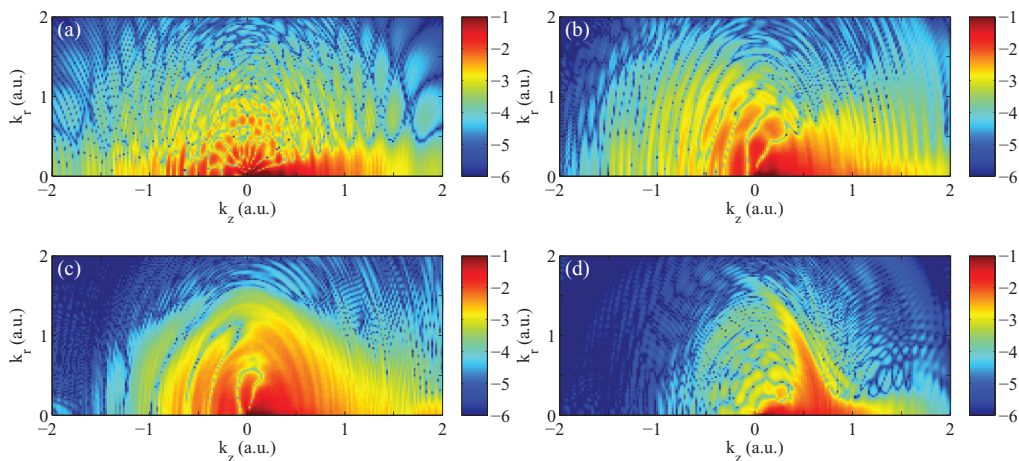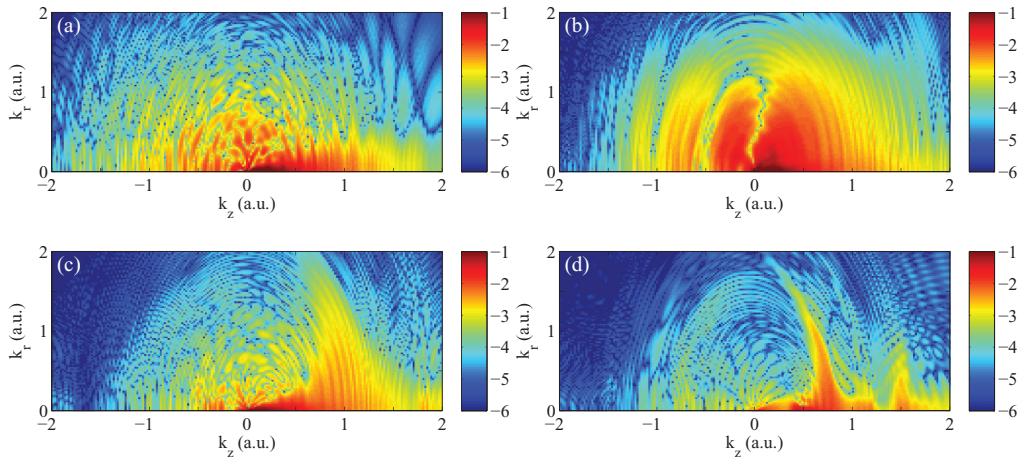

FIG. 9. (Color online) Idem Fig. 8 but for $\phi = \pi/2$.

FIG. 10. (Color online) Idem Fig. 8 but for $\phi = \pi$.

the forward-backward asymmetry or two-dimensional electron momentum distributions, should complement the $P(E)$ measurements [1]. Furthermore, the utilization of nonhomogeneous fields would open the avenue for the production of high-energy electrons, reaching the keV regime, if a reliable control of the spatial and temporal shape of the laser electric field is attained. Investigations in such direction have already started (see, e.g., [29] and references therein).

A deep analysis of the electron distributions for atomic ionization produced by an external laser field can be performed in terms of the two-dimensional electron momentum distribution. The exact solution of the three-dimensional Schrödinger equation (3D-TDSE) provides us with an excellent tool to analyze in detail how the two competing fields, namely the laser electric field and the Coulomb atomic potential, modify the electron wave packet of the laser released electron. In Figs. 4–7 we calculate two-dimensional electron momentum distribution for a laser field with an intensity of $I = 1.140 \times 10^{14}$ W/cm^2 ($E_0 = 0.057$ a.u), $\lambda = 800$ nm, and different values of the the β parameter: (a) $\beta = 0$ (homogeneous case), (b) $\beta = 0.002$, (c) $\beta = 0.003$, and (d) $\beta = 0.005$. We employ a few-cycle laser pulse with four total cycles (10 fs) and various values of the carrier envelope phase (CEP) parameter

ϕ, namely $\phi = 0$ (Fig. 4), $\phi = \pi/2$ (Fig. 5), $\phi = \pi$ (Fig. 6), and $\phi = 3\pi/2$ (Fig. 7), respectively.

Here we concentrate our analysis on the low energy region of the distributions in order to study how the inhomogeneities of the laser electric field affect the angular electron yield. This region shows the usual *bouquet*-type structures (see [11] for details) with noticeable modifications for all the nonhomogeneous cases studied.

Furthermore, the low-energy electrons appear to be strongly influenced by the spatial inhomogeneity of the laser electric field [see (b)–(d) of Figs. 4–7]. We also can observe how the *bouquet* structures present in the homogeneous case *disappear* for particular values of ϕ [see, e.g., Fig. 6(d)].

In order to complete our investigations, we calculate two-dimensional electron momentum distributions by increasing the laser field intensity to $I = 5.0544 \times 10^{14}$ W/cm^2 ($E_0 = 0.12$ a.u). The results are depicted in Figs. 8–11 for $\phi = 0$, $\phi = \pi/2$, $\phi = \pi$, and $\phi = 3\pi/2$, respectively. Here (a), (b), (c), and (d) represent the cases with $\beta = 0$ (homogeneous case), $\beta = 0.002$, $\beta = 0.003$, and $\beta = 0.005$, respectively.

Following the trend observed in the previous studied case, we see strong modifications produced by the spatial inhomogeneities in both the angular and low-energy structures.
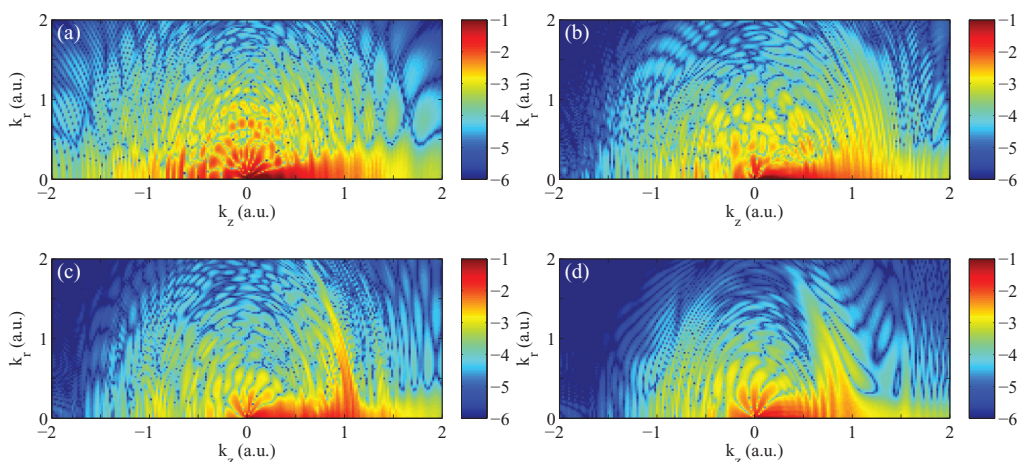
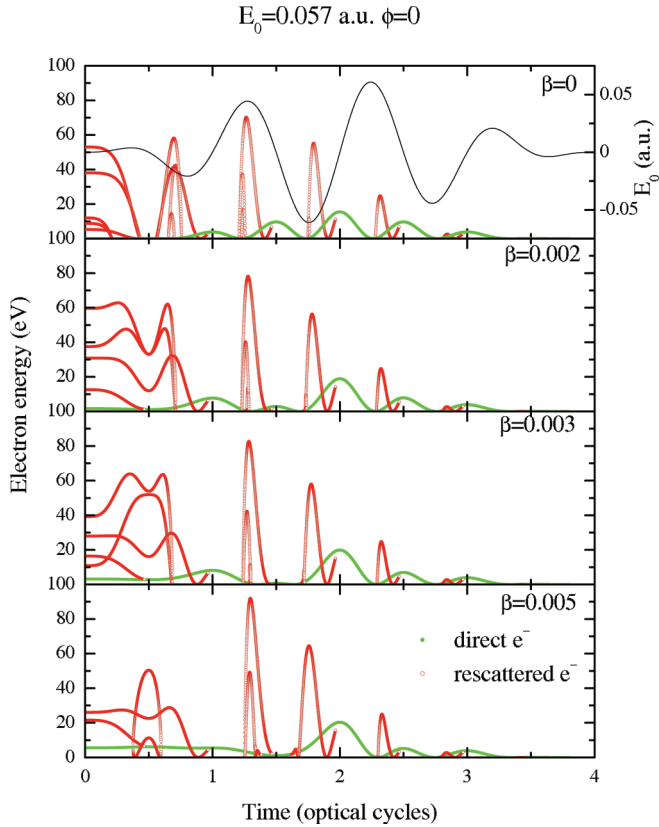FIG. 11. (Color online) Idem Fig. 8 but for $\phi = 3\pi/2$.

E_0=0.057 a.u. ϕ=0

E_0=0.057 a.u. ϕ=π/2

FIG. 12. (Color online) Numerical solutions of the Newton equation [Eq. (9)] plotted in terms of the direct and rescattered electron kinetic energy E_k^d and E_k^r, respectively. The laser parameters are $I = 1.140 \times 10^{14}$ W/cm^2 ($E_0 = 0.057$ a.u), $\lambda = 800$ nm, and $\phi = 0$. We employ a few-cycle laser pulse with four total cycles (10 fs). The temporal shape of the laser electric field is superimposed in the top panel. Different panels correspond to various values of β (see labels). Green filled circles: *direct* electrons; red empty circles: *rescattered* electrons.

FIG. 13. (Color online) Idem Fig. 12 for $\phi = \pi/2$.

Indeed, the change seems to be even more pronounced. For instance, the yield for electrons with $k_z < -1$ a.u. for $\phi = 0$ [Fig. 8(d)] and $\phi = \pi/2$ [Fig. 9(d)] drops several orders of magnitude in evident contrast with the yield for $k_z > 0$ a.u. This significant difference between the above mentioned yields would open a new approach to characterize the CEP of few-cycle laser pulses using spatially nonhomogeneous fields.

We now employ a classical model in order to explain and characterize the extension of the energy-resolved photoelectron spectra. According to the simple-man's model [53] the physical mechanism behind the ATI process can be understood as follows: At a given time, that we call ionization time t_i, an atomic electron is released or *born* at the position $z = 0$ (i.e., where the atom is located) with zero velocity, i.e., $\dot{z}(t_i) = 0$. This electron now moves only under the influence of the oscillating laser electric field (this model neglects the Coulomb interaction with the remaining ion) and will reach the detector either directly or through the process known as rescattering. By using the classical equation of motion of an electron moving in an oscillating electric field, it is possible to calculate the maximum *classical* kinetic energy of the electron for both the direct and rescattered processes.
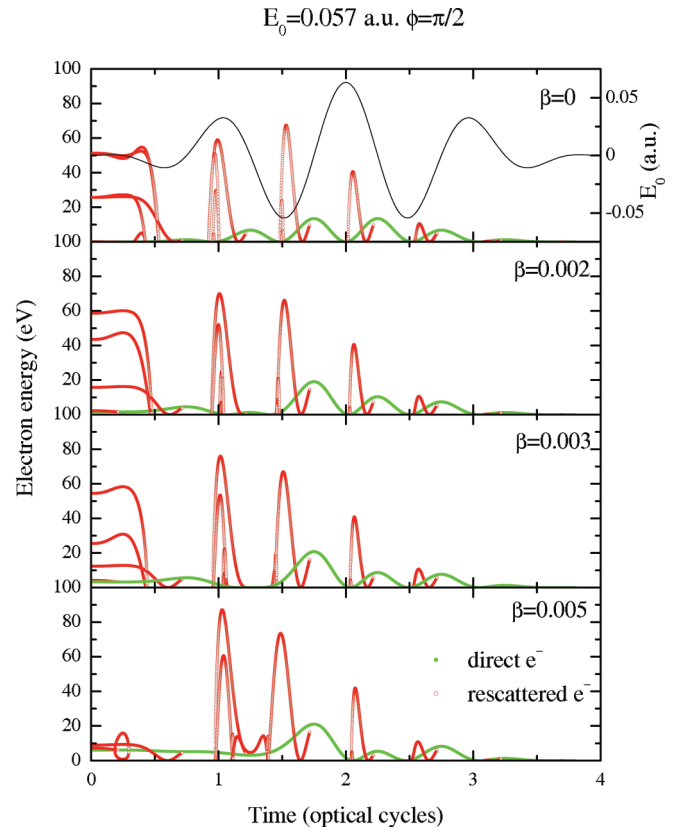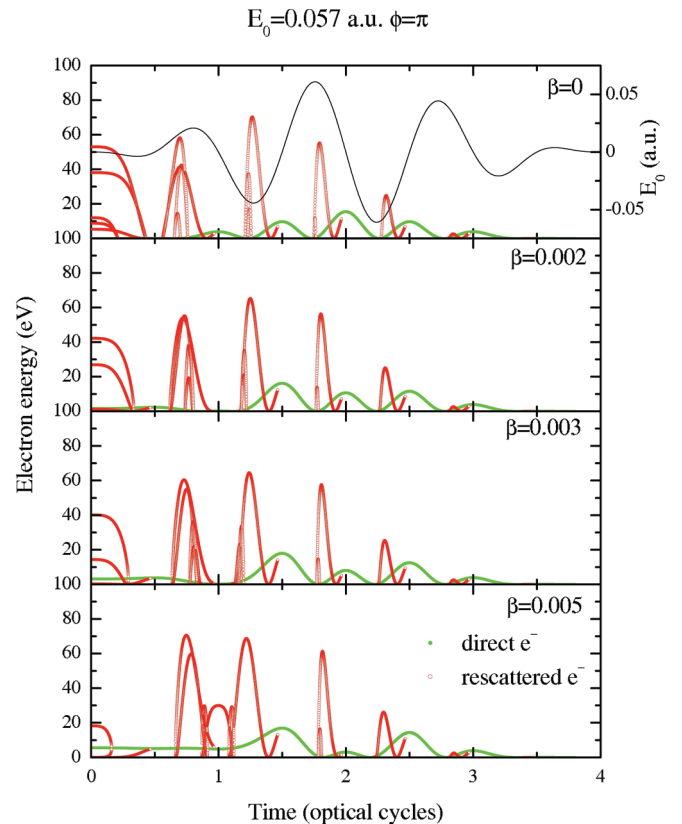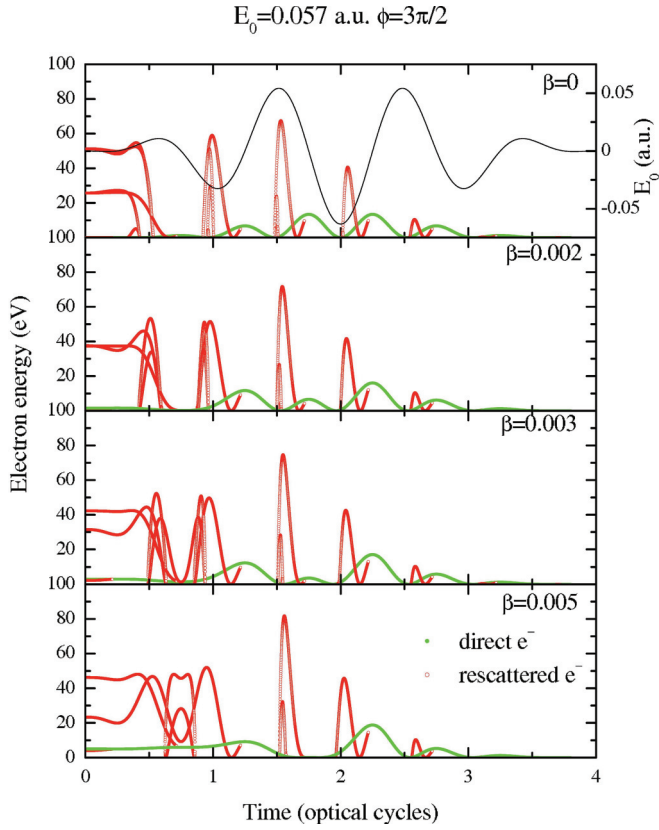

E_0=0.057 a.u. ϕ=π

FIG. 14. (Color online) Idem Fig. 12 for $\phi = \pi$.

FIG. 15. (Color online) Idem Fig. 12 for $\phi = 3\pi/2$.

The Newton equation of motion for the atomic electron in the laser electric field can be written, using the functional form of Eq. (3), as follows:

$$\ddot{z}(t) = -\nabla_z V_l(\mathbf{r},t), \tag{9}$$

$$\ddot{z}(t) = E(t)[1 + 2\beta z(t)], \tag{10}$$

where we have collected the time-dependent part of the electric field in $E(t)$, i.e., $E(t) = E_0 f(t) \sin(\omega t + \phi)$.

In the limit where $\beta = 0$ in Eq. (9), we recover the homogeneous case [1]. For the direct laser ionization, the kinetic energy of an electron released or born at time t_i is

$$E_k^d = \frac{[\dot{z}(t_i) - \dot{z}(t_f)]^2}{2}, \tag{11}$$

where t_f is the end time of the laser pulse. For the rescattered laser-ionized electron, in which the electron returns to the core at a time t_r and reverses its direction, the kinetic energy of the electron yields

$$E_k^r = \frac{[\dot{z}(t_i) + \dot{z}(t_f) - 2\dot{z}(t_r)]^2}{2}. \tag{12}$$

For homogeneous fields, Eqs. (11) and (12) become the usual expressions $E_k^d = \frac{[A(t_i) - A(t_f)]^2}{2}$ and $E_k^r = \frac{[A(t_i) + A(t_f) - 2A(t_r)]^2}{2}$, with $A(t)$ being the laser vector potential $A(t) = -\int^t E(t')dt'$, respectively. For the case with $\beta = 0$, it can be shown that the maximum value for E_k^d is $2U_p$, while for E_k^r it is $10U_p$ [1]. These two values appear as cutoffs in the
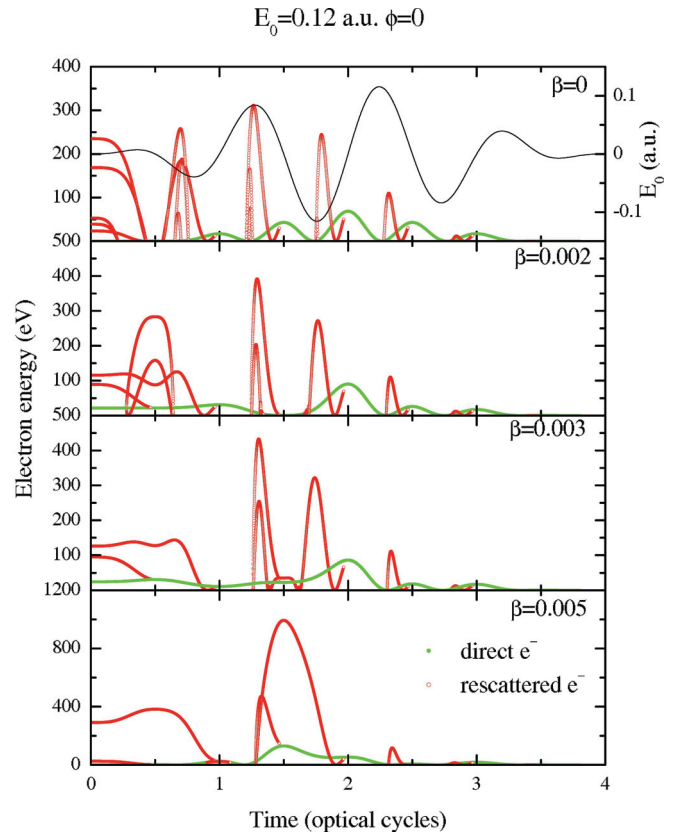

FIG. 16. (Color online) Numerical solutions of the Newton equation [Eq. (9)] plotted in terms of the direct and rescattered electron kinetic energy E_k^d and E_k^r, respectively. The laser parameters are $I = 5.0544 \times 10^{14}$ W/cm² ($E_0 = 0.12$ a.u.), $\lambda = 800$ nm, and $\phi = 0$. We employ a few-cycle laser pulse with four total cycles (10 fs). The temporal shape of the laser electric field is superimposed in the top panel. Different panels correspond to various values of β (see labels). Green filled circles: *direct* electrons; red empty circles: *rescattered* electrons.

energy-resolved photoelectron spectrum as can be observed in Figs. 2(a) and 3(a).

In Figs. 12–19, we present the numerical solutions of Eq. (9), which is plotted in terms of the kinetic energy (in eV) of the direct (green filled circles) and rescattered (red empty circles) electrons.

Figures 12–15 are for a laser intensity of $I = 1.140 \times 10^{14}$ W/cm² ($E_0 = 0.057$ a.u.), meanwhile in Figs. 16–19 the laser intensity is $I = 5.404 \times 10^{14}$ W/cm² ($E_0 = 0.12$ a.u.). Figures 12(16), 13(17), 14(18), and 15(19) are for $\phi = 0$, $\phi = \pi/2, \phi = \pi$, and $\phi = 3\pi/2$, respectively, and for different values of the β parameter [$\beta = 0$ (homogeneous case), $\beta = 0.002$, $\beta = 0.003$, and $\beta = 0.005$, from top to bottom]. We have included in the top panels of all the figures the temporal shape of the laser electric field.

From the curves for $\beta \neq 0$ we can observe the strong modifications that the nonhomogeneous character of the laser electric field produces in the kinetic energy of the laser-ionized electron. Furthermore, it is possible to observe how the kinetic energy is more sensitive to the CEP. If we analyze, for instance, the top panels of Figs. 12–15 (i.e., the homogeneous case) we conclude that the shape of both the kinetic energy of
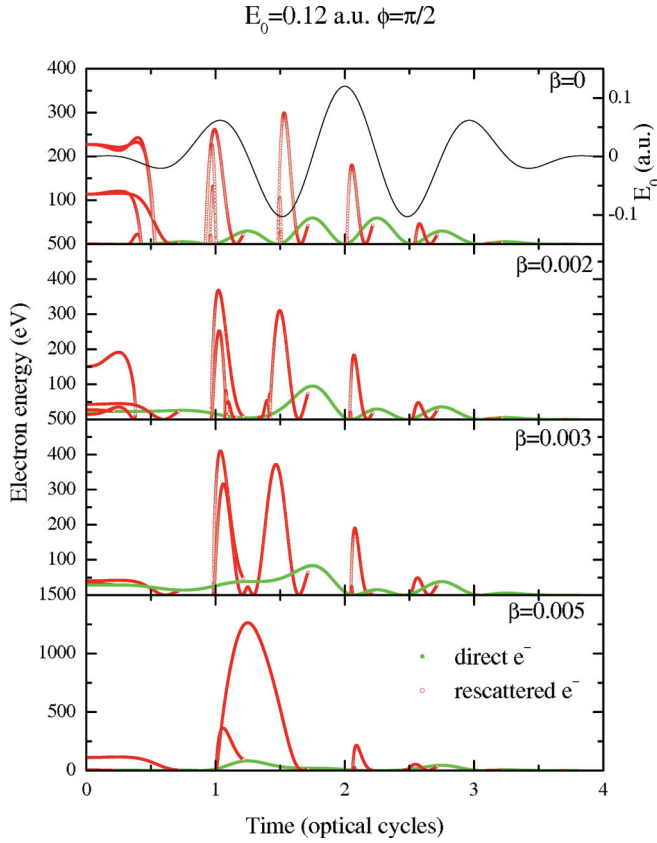
FIG. 17. (Color online) Idem Fig. 16 for $\phi = \pi/2$.
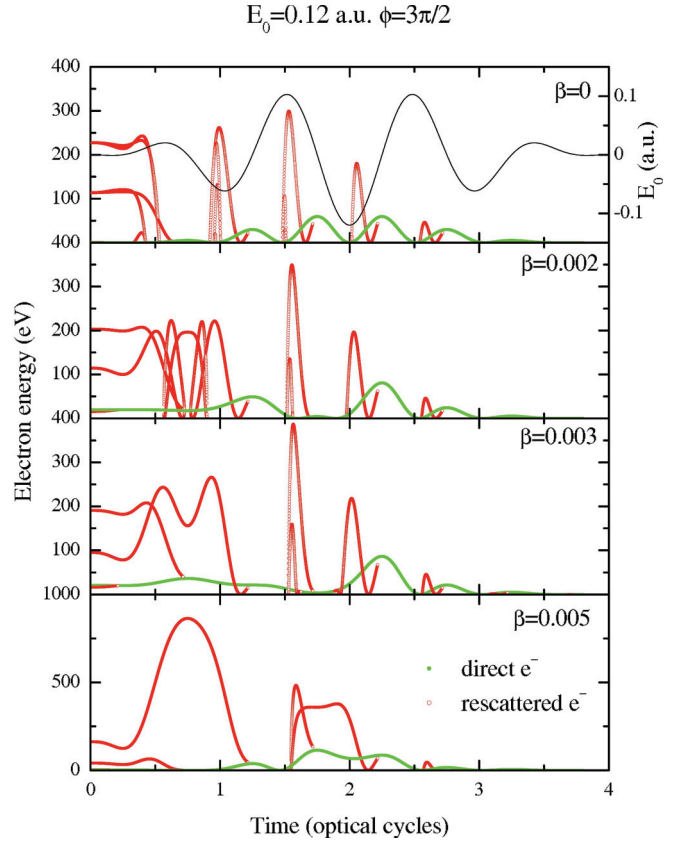
FIG. 19. (Color online) Idem Fig. 16 for $\phi = 3\pi/2$.
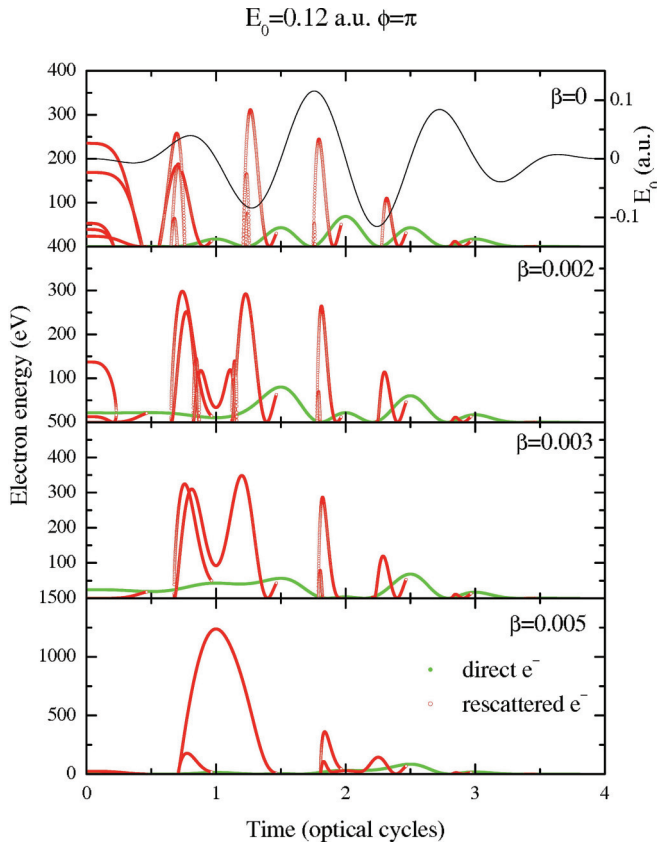
FIG. 18. (Color online) Idem Fig. 16 for $\phi = \pi$.

the direct and rescattered electron are identical for $\phi = 0$ ($\phi = \pi/2$) and $\phi = \pi$ ($\phi = 3\pi/2$). On the other hand, for the different values of β the kinetic energy has a unique shape for a given value of ϕ. A similar behavior, both for the homogeneous and nonhomogeneous cases, was indeed observed in the photoelectron spectra calculated using the 3D-TDSE (see Figs. 2 and 3) as well.

The particular features present for $\beta \neq 0$ are related to the changes in the laser-ionized electron trajectories (for details see, e.g., [37–39]). In summary, the electron trajectories are modified in such a way that now the electron ionizes at an earlier time and recombines later, and in this way it spends more time in the continuum acquiring energy from the laser electric field. Consequently, higher values of the kinetic energy are attained. This distinct behavior is more evident for $E_0 = 0.12$ a.u. and $\beta = 0.005$, but it appears to some extent for all the studied cases.

A similar behavior was observed recently in the so-called above-threshold photoemission (ATP) using metal nanotips. According to the model developed in Ref. [31] the strong localized fields modify the electron motion in such a way to allow subcycle dynamics.

In our approach, however, we include the full picture of the ATI phenomenon, namely both direct and rescattered electrons are considered (in Ref. [31] only direct electrons are taken into account) and consequently the characterization of the dynamics of the photoelectrons is more complex. Nevertheless, the higher kinetic energy of the rescattered electrons is a clear consequence of the strong modifications the
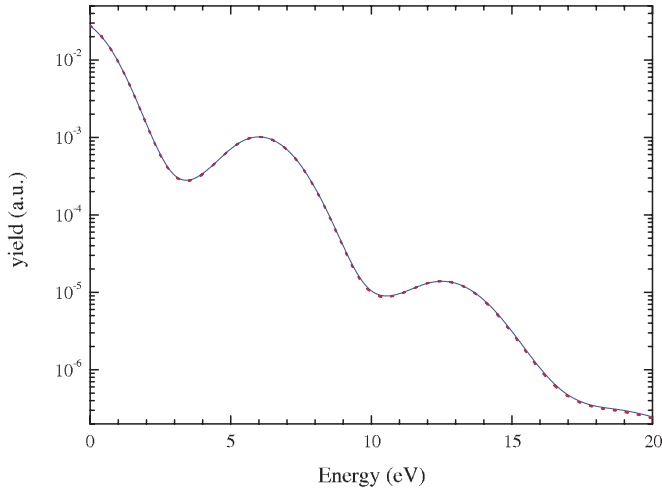
FIG. 20. (Color online) Energy-resolved photoelectron spectra $P(E)$ calculated using the 3D-TDSE for an hydrogen atom ($I_p = -0.5$ a.u.). The laser parameters are $E_0 = 0.05$ a.u. ($I = 8.775 \times 10^{13}$ W/cm^2) and $\omega = 0.25$ a.u. ($\lambda = 182.5$ nm). We have used a sin-squared shaped pulse with a total duration of six optical cycles (3.7 fs) and $\phi = \pi/2$. Solid blue line: homogeneous case ($\beta = 0$); dotted red line: $\beta = 0.005$. We note that both lines are practically on top of each other (see text for details).

laser electric field produces in the region where the electron dynamics takes place, as in the above mentioned case of ATP.

B. Multiphoton regime

For the multiphoton case we consider a few-cycle laser pulse with six complete optical cycles and $E_0 = 0.05$ a.u. ($I = 8.775 \times 10^{13}$ W/cm^2) and $\omega = 0.25$ a.u. ($\lambda = 182.5$ nm). In here the Keldysh parameter is $\gamma = 5$, indicating the

predominance of the multiphoton process [11]. We have computed the $P(E)$, two-dimensional electron distributions and the classical electron energies for all the set of cases presented in Sec. III A. In this paper, however, we just present the most extreme case with $\beta = 0.005$ and CEP of $\phi = \pi/2$. These results are presented in Figs. 20–22 for $P(E)$, two-dimensional electron distributions, and the classical electron kinetic energies, respectively. The $P(E)$ exhibits the usual multiphoton peaks [2,48] and the inhomogeneity of the field does not play any significant role. In the whole range, the values of the yields have a difference of less than 5% and in the logarithmic scale used this is hard to discern and consequently only one line is visible.

The two-dimensional electron distributions are also the same in terms of shape and magnitude for the both homogeneous and inhomogeneous cases, as shown in both panels of Fig. 21. It means the differences introduced by the spatial nonhomogeneous character are practically imperceptible. We should note that our calculation is basically identical to the one presented in [11].

The numerical solutions of Eq. (9) as function of the kinetic energy (in eV) of the direct and rescattered electron is depicted in Fig. 22. In here we could also observe, in support to our quantum mechanical calculations, that the inhomogeneity of the laser field does not change the electron energies in both the direct and rescattered processes.

In general, we do not find noticeable differences in these observable quantities for both variations in the CEP and the strength of the inhomogeneity parameter β. As a result, we conclude that in the multiphoton regime the modifications introduced by the spatial inhomogeneities of the laser electric field do not produce appreciable modifications in the electron dynamics and consequently in the measurable quantities. In addition, the laser-ionized electron, in both the direct and
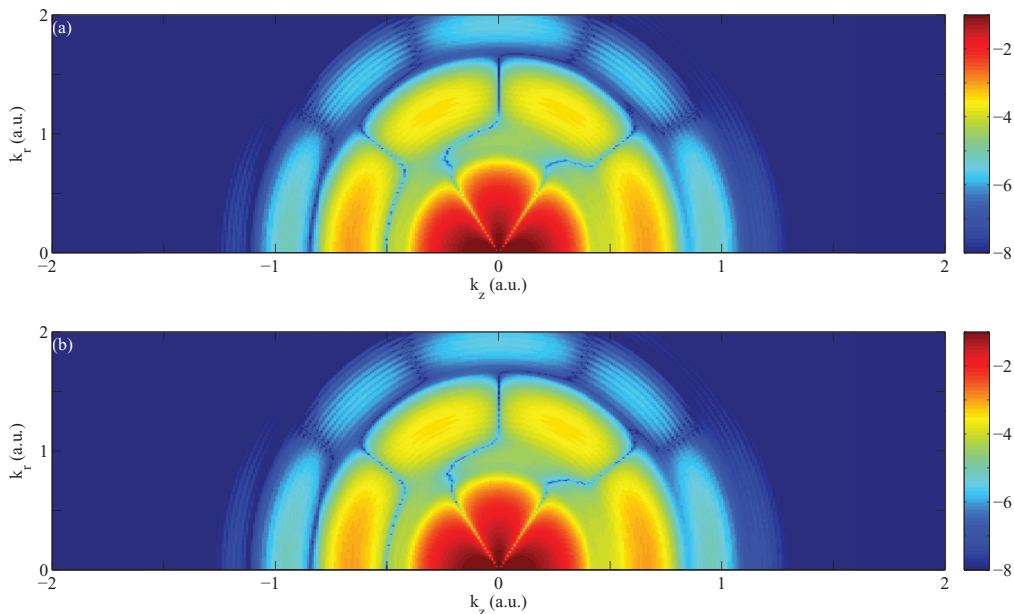

FIG. 21. (Color online) Two-dimensional electron momentum distributions (logarithmic scale) in cylindrical coordinates (k_z, k_r) using the exact 3D-TDSE calculation for an hydrogen atom. The laser parameters are $E_0 = 0.05$ a.u. ($I = 8.775 \times 10^{13}$ W/cm^2), $\omega = 0.25$ a.u. ($\lambda = 182.5$ nm), and $\phi = \pi/2$. We employ a few-cycle laser pulse with six total optical cycles (3.7 fs). (a) Homogeneous case ($\beta = 0$) and (b) is for $\beta = 0.005$.
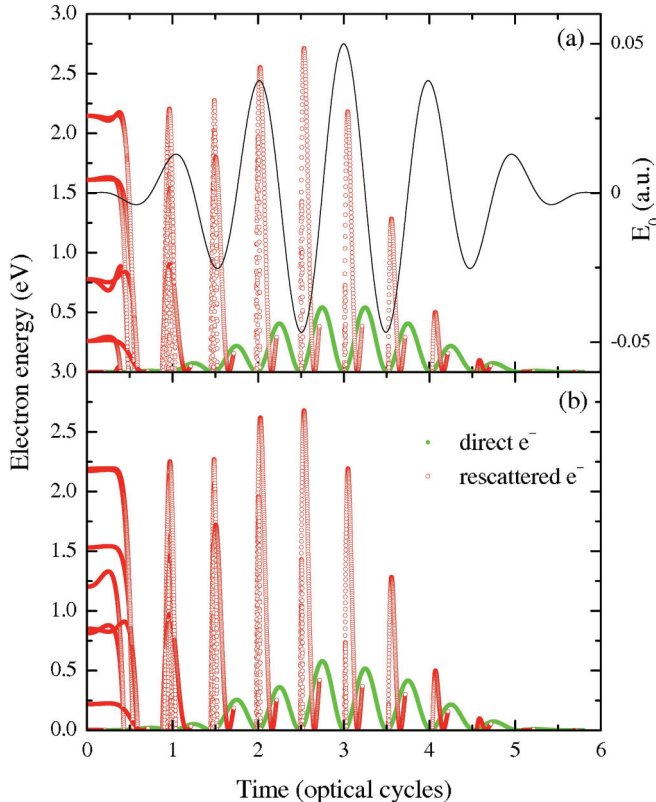
FIG. 22. (Color online) Numerical solutions of the Newton equation [Eq. (9)] plotted in terms of the direct and rescattered electron kinetic energy E_k^d and E_k^r, respectively. The laser parameters are $E_0 = 0.05$ a.u. ($I = 8.775 \times 10^{13}$ W/cm^2), $\omega = 0.25$ a.u. ($\lambda = 182.5$ nm), and $\phi = \pi/2$. We employ a few-cycle laser pulse with six total cycles (3.7 fs). The temporal shape of the laser electric field is superimposed in (a). (a) Homogeneous case ($\beta = 0$) and (b) is for $\beta = 0.005$. Green filled circles: *direct* electrons; red empty circles: *rescattered* electrons.

rescattered processes, has a very small kinetic energy in the multiphoton regime due to a lower value of its ponderomotive energy ($U_p = 0.01$ a.u.). Indeed, in this case the maximum energy after the rescattering process has taken place is ≈3 eV. As a result, it is reasonable to have a very small or almost no differences between the final kinetic energies, when a spatial inhomogeneity of small strength is present.

IV. CONCLUSIONS AND OUTLOOK

We have extended our previous studies of above-threshold ionization (ATI) produced by spatially nonhomogeneous fields using the three-dimensional solutions of the time-dependent Schrödinger equation (3D-TDSE). We have modified the 3D-TDSE to model the ATI phenomenon driven by spatial nonhomogeneous fields by including an additional term in the laser-electron coupling. In the tunneling regime ($\gamma \lesssim 1$) we predict an extension in the conventional cutoffs position and an increase of the yield of the energy-resolved photoelectron spectra in certain regions. In addition, both the photoelectron spectra $P(E)$ and the two-dimensional electron momentum distributions appear to be more sensitive to the carrier envelope phase of the laser electric field. This feature indicates that the photoelectrons produced by spatial inhomogeneous field could be a good candidate for few-cycle laser pulses characterization. Furthermore, our predictions pave the way for the production of high-energy photoelectrons, reaching the keV regime, using plasmon enhanced fields. In the multiphoton regime ($\gamma \gg 1$), on the other hand, we show that both the $P(E)$ and the two-dimensional electron distributions are hardly affected by the spatial nonhomogeneities of the laser electric field. Our quantum mechanical calculations are supported by the classical simulations. In particular, the $P(E)$ characteristics are reasonably well reproduced by simulations based on classical physics.

[1] D. B. Milošević, G. G. Paulus, D. Bauer, and W. Becker, J. Phys. B **39**, R203 (2006).

[2] P. Agostini, F. Fabre, G. Mainfray, G. Petite, and N. K. Rahman, Phys. Rev. Lett. **42**, 1127 (1979).

[3] M. Schnürer, C. Streli, P. Wobrauschek, M. Hentschel, R. Kienberger, C. Spielmann, and F. Krausz, Phys. Rev. Lett. **85**, 3392 (2000).

[4] P. von den Hoff, I. Znakovskaya, M. Kling, and R. de Vivie-Riedle, Chem. Phys. **366**, 139 (2009).

[5] F. Ferrari, F. Calegari, M. Lucchini, C. Vozzi, S. Stagira, G. Sansone, and M. Nisoli, Nat. Phot. **4**, 975 (2010).

[6] M. Schultze, E. Goulielmakis, M. Uiberacker, M. Hofstetter, J. Kim, D. Kim, F. Krausz, and U. Kleineberg, New J. Phys. **9**, 243 (2007).

[7] J. Ullrich, R. Moshammer, R. Dörner, O. Jagutzki, V. Mergel, H. Schmidt-Böcking, and L. Spielberger, J. Phys. B **30**, 2917 (1997).

[8] A. Rudenko, K. Zrost, C. D. Schröter, V. L. B. de Jesus, B. Feuerstein, R. Moshammer, and J. Ullrich, J. Phys. B **37**, L407 (2004).

[9] C. M. Maharjan, A. S. Alnaser, I. Litvinyuk, P. Ranitovic, and C. L. Cocke, J. Phys. B **39**, 1955 (2006).

[10] M. Schuricke, G. Zhu, J. Steinmann, K. Simeonidis, I. Ivanov, A. Kheifets, A. N. Grum-Grzhimailo, K. Bartschat, A. Dorn, and J. Ullrich, Phys. Rev. A **83**, 023413 (2011).

[11] D. G. Arbó, J. E. Miraglia, M. S. Gravielle, K. Schiessl, E. Persson, and J. Burgdörfer, Phys. Rev. A **77**, 013401 (2008).

[12] T. Wittmann, B. Horvath, W. Helml, M. G. Schätzel, X. Gu, A. L. Cavalieri, G. G. Paulus, and R. Kienberger, Nat. Phys. **5**, 357 (2009).

[13] M. F. Kling, J. Rauschenberger, A. J. Verhoef, D. B. M. E. Hasović, T. Uphues, H. G. Muller, and M. J. J. Vrakking, New J. Phys. **10**, 025024 (2008).

[14] M. Nisoli, G. Sansone, S. Stagira, S. De Silvestri, C. Vozzi, M. Pascolini, L. Poletto, P. Villoresi, and G. Tondello, Phys. Rev. Lett. **91**, 213905 (2003).

[15] G. G. Paulus, F. Grasbon, H. Walther, P. Villoresi, M. Nisoli, S. Stagira, E. Priori, and S. D. Silvestri, Nature (London) **414**, 182 (2001).

[16] X. Liu, H. Rottke, E. Eremina, W. Sandner, E. Goulielmakis, K. O. Keeffe, M. Lezius, F. Krausz, F. Lindner, M. G. Schätzel *et al.*, Phys. Rev. Lett. **93**, 263001 (2004).

[17] A. M. Sayler, T. Rathje, M. Moller, D. Hoff, G. Stibenz, W. Müller, C. Kurbis, K. Rühle, and G. G. Paulus, *CLEO EUROPE/EQEC* (Optical Society of America, Washington, DC, 2011), p. 1.

[18] A. M. Sayler, T. Rathje, W. Müller, K. Rühle, R. Kienberger, and G. G. Paulus, Opt. Lett. **36**, 1 (2011).

[19] D. B. Milošević, G. G. Paulus, and W. Becker, Phys. Rev. Lett. **89**, 153001 (2002).

[20] G. G. Paulus, F. Lindner, H. Walther, A. Baltuška, E. Goulielmakis, M. Lezius, and F. Krausz, Phys. Rev. Lett. **91**, 253004 (2003).

[21] S. Kim, J. Jin, Y.-J. Kim, I.-Y. Park, Y. Kim, and S.-W. Kim, Nature (London) **453**, 757 (2008).

[22] I.-Y. Park, S. Kim, J. Choi, D.-H. L. Y.-J. Kim, M. F. Kling, M. I. Stockman, and S.-W. Kim, Nat. Phot. **5**, 677 (2011).

[23] M. Sivis, M. Duwe, B. Abel, and C. Ropers, Nature (London) **485**, E1 (2012).

[24] S. Kim, J. Jin, Y.-J. Kim, I.-Y. Park, Y. Kim, and S.-W. Kim, Nature (London) **485**, E2 (2012).

[25] S. Zherebtsov *et al.*, Nat. Phys. **7**, 656 (2011).

[26] M. Krüger, M. Schenk, and P. Hommelhoff, Nature (London) **475**, 78 (2011).

[27] P. Hommelhoff, Y. Sortais, A. Aghajani-Talesh, and M. A. Kasevich, Phys. Rev. Lett. **96**, 077401 (2006).

[28] M. Schenk, M. Krüger, and P. Hommelhoff, Phys. Rev. Lett. **105**, 257601 (2010).

[29] M. Krüger, M. Schenk, M. Förster, and P. Hommelhoff, J. Phys. B **45**, 074006 (2012).

[30] P. Dombi, P. Racz, J. Fekete, A. Thai, S. Teichmann, O. Chalus, P. K. Bates, and J. Biegert, *Lasers, and Electro-Optics (CLEO), 2011 Conference* (Optical Society of America, Washington, DC, 2011), pp. 1–2.

[31] G. Herink, D. R. Solli, M. Gulde, and C. Ropers, Nature (London) **483**, 190 (2012).

[32] A. Apolonski *et al.*, Phys. Rev. Lett. **92**, 073902 (2004).

[33] P. Dombi, P. Racz, and B. Bodi, Laser Part. Beams **27**, 291 (2009).

[34] M. Protopapas, C. H. Keitel, and P. L. Knight, Rep. Prog. Phys. **60**, 389 (1997).

[35] T. Brabec and F. Krausz, Rev. Mod. Phys. **72**, 545 (2000).

[36] A. Husakou, S.-J. Im, and J. Herrmann, Phys. Rev. A **83**, 043839 (2011).

[37] M. F. Ciappina, J. Biegert, R. Quidant, and M. Lewenstein, Phys. Rev. A **85**, 033828 (2012).

[38] I. Yavuz, E. A. Bleda, Z. Altun, and T. Topcu, Phys. Rev. A **85**, 013416 (2012).

[39] M. F. Ciappina, S. S. Aćimović, T. Shaaran, J. Biegert, R. Quidant, and M. Lewenstein, Opt. Exp. **20**, 26261 (2012).

[40] M. F. Ciappina, J. A. Pérez-Hernández, T. Shaaran, J. Biegert, R. Quidant, and M. Lewenstein, Phys. Rev. A **86**, 023413 (2012).

[41] T. Shaaran, M. F. Ciappina, and M. Lewenstein, Phys. Rev. A **86**, 023408 (2012).

[42] T. Shaaran, M. F. Ciappina, and M. Lewenstein, J. Mod. Opt. **59**, 1634 (2012).

[43] K. J. Schafer, B. Yang, L. F. DiMauro, and K. C. Kulander, Phys. Rev. Lett. **70**, 1599 (1993).

[44] D. A. Telnov and S.-I. Chu, Phys. Rev. A **79**, 043421 (2009).

[45] D. Bauer and P. Koval, Comp. Phys. Commun. **174**, 396 (2006).

[46] C. I. Blaga, F. Catoire, P. Colosimo, G. G. Paulus, H. G. Muller, P. Agostini, and L. F. DiMauro, Nat. Phys. **5**, 335 (2009).

[47] W. Quan, Z. Lin, M. Wu, H. Kang, H. Liu, X. Liu, J. Chen, J. Liu, X. T. He, S. G. Chen *et al.*, Phys. Rev. Lett. **103**, 093001 (2009).

[48] K. J. Schafer and K. C. Kulander, Phys. Rev. A **42**, 5794 (1990).

[49] K. J. Schafer, Comp. Phys. Commun. **63**, 427 (1991).

[50] K. J. Schafer, in *Strong Field Laser Physics*, edited by T. Brabec, Springer Series in Optical Sciences (Springer, Berlin, 2008).

[51] H. R. Reiss, Phys. Rev. A **75**, 031404(R) (2007).

[52] H. R. Reiss, Phys. Rev. A **82**, 023418 (2010).

[53] P. B. Corkum, Phys. Rev. Lett. **71**, 1994 (1993).